

Global piston restoration of segmented mirrors with convolutional recurrent neural network approach

DAILOS GUERRA-RAMOS^{1,*}, JUAN TRUJILLO-SEVILLA², AND JOSE MANUEL RODRÍGUEZ-RAMOS^{2,3}

¹Universidad de La Laguna. C/ Padre Herrera s/n. 38200, La Laguna. Tenerife. Canary Islands. Spain

²Wooptix, S.L. Avda. Trinidad 61. 38204, La Laguna. Tenerife. Canary Islands. Spain

³Cibican. Campus Ciencias de La Salud s/n, E-38071 La Laguna. Spain

*Email: dailos.guerra@gtc.iac.es

Compiled March 7, 2019

Machine learning has been applied successfully in many fields. Two families of neural networks namely convolutional and recurrent, are employed in this paper to deal with the phasing of segmented mirrors. These families are specialized in finding patterns in a grid of values such as images and sequential data respectively. The two combined gives robustness as well as accuracy in predicting global piston values for each of the segments. Four wavelengths were used to unravel the ambiguity. Atmospheric seeing, polishing and tip-tilt residual errors were added in the simulations. © 2019 Optical Society of America

OCIS codes: (100.4996) Pattern recognition, neural networks; (100.5070) Phase retrieval; (120.5050) Phase measurement; (120.6085) Space instrumentation.

<http://dx.doi.org/10.1364/ao.XX.XXXXXX>

In the quest of building bigger telescopes, monolithic mirrors were dumped in favor of segmented ones easier to fabricate and maintain. However, this partition in the reflective surface carries the necessity of the alignment of the constituents parts with high precision. Particularly, when adaptive optics systems are present, this procedure becomes very demanding. Under these circumstances, the phase difference between segments must be below a small fraction of the wavelength.

Several methods have been proposed for treating this problem adequately. Nowadays, all the methods used for cophasing segmented mirrors in main telescopes are based on Shack-Hartman wavefront sensors [1] [2]. They are robust and precise but require to align microlenses or prisms with every edge of the segments which is very time consuming and might become impractical for a growing number of segments. There is other category of methods that are hinge on Curvature wavefront sensors [3] [4]. They have been used traditionally for crosschecking the measurement of the primary method. They lack a very wide capture range and are very sensible to atmospheric conditions. Nonetheless, they provide a very simple optical design and require no special hardware.

The method we will discuss in the following paper cannot be fit in any of the two previously alluded categories. This is

because only one image recorded at a single defocused distance is needed in order to operate. This image must be taken at four different wavelengths, the exact four that were used in the training of the network.

Neural network applications for wavefront sensing are not new [5]. The potential use behind them as a universal approximation algorithm is well known from time ago. However the field has seen a recent rise due in part to the increase in computing power and the amount of available data. It has been applied convolutional neural networks alone before to extract relative piston values between segments [6]. Those methods were unstable in the presence of many sources of error. We will show here an architecture that uses convolutional and recurrent neural networks to extract features from diffraction images of the junctions of the segments and from the relation among neighbouring junctions. Mixing this techniques allows the algorithm to give more precise predictions and ample capture range with more robustness and fewer number of wavelengths.

We will organize this paper in the following manner. First we will give a brief introduction about the physical background of the problem and some mathematical considerations. We continue with the optical setup needed and the simulation process we follow to create the data images to feed the network. We then proceed to explain the details of the network architecture. Next, some insights about the learning process are explained. Eventually, conclusions, future works and final remarks are found at the end of paper.

Ideally the electromagnetic field that arises from a distant star reaches the pupil of the telescope as a plane wave. Atmospheric turbulence and irregularities in the mirror surface will make the wavefront depart from this perfect planar view. We now make a distinction between irregularities that are discontinuous i.e. piston, and continuous e.g. polishing errors, tip-tilt.

The difficulty of the detection of the piston misalignment lies in the intrinsic ambiguity that conveys the periodicity of an electromagnetic wave. That attribute of monochromatic light makes indistinguishable optical paths that are a multiple of 2π radians away. Lets think of an ideal scenario of a planar wave partitioned into two half-planes with a different phase each. There is then a discontinuous phase jump, $\Delta\phi$, along a line that produces a distinct diffraction pattern when propagating a distance z . This pattern repeats every 2π , i.e. for a given

wavelength and a given phase jump $\phi_0 \in [0, 2\pi]$, the patterns produced by $\Delta\phi = n2\pi + \phi_0$ are equivalent for any $n \in \mathbb{N}$. The diffraction patterns that we need to simulate for our purposes comes from a wavefront that contains hexagonal phase jumps of this kind, i.e. a plane wave that reflects in a segmented mirror of the telescope that is not properly phased [7].

The diffraction pattern produced by a discontinuous phase jump has another interesting property to notice: phase jumps of $\Delta\phi = +\phi_0$ are a reversed version of $\Delta\phi = -\phi_0$ for any $\phi_0 \in [0, 2\pi]$. These two periodicities are going to be considered in the training of the network.

The light beam being reflected in a segmented mirror telescope is not collimated but a spherical wave converging to the focus. The propagation distance to the conjugate plane is related to f , the focus distance and l , the distance between focal plane and defocused plane (where the detector is placed) in the following way:

$$z = \frac{(f-l)f}{l}. \quad (1)$$

We choose a propagation distance such that the full peak width of the diffraction pattern so generated at the defocused image plane should be some factor, ξ_σ , larger than the image blur due to the turbulence. As explained in [8]:

$$z < \frac{0.8 \cdot r_0^2}{\lambda_{r_0}^{12/5}} \cdot \xi_\sigma^{-2} \cdot \lambda^{7/5}, \quad (2)$$

where $\lambda_{r_0} = 500$ nm is the wavelength at which the atmospheric seeing is measured, r_0 is the Fried parameter and λ is the wavelength used. A reasonable factor value is $\xi_\sigma = 2$.

To propagate the wavefront a distance z we use Fresnel equation in its convolutional form as is presented here:

$$U(x, y) \propto \mathcal{F}^{-1} \{ U(\xi, \eta) e^{-i\pi\lambda z(f_\xi^2 + f_\eta^2)} \}, \quad (3)$$

where f_x, f_y are coordinates in frequency domain, the complex amplitude field at the pupil is $U(\xi, \eta)$ and the complex amplitude field at a distance z is represented by $U(x, y)$.

But we are actually interested in the intensity image, so we compute the square of the magnitude of the complex field obtain in equation 3.

In order to create the simulations needed to feed the network we use the parameters included in table 1 for a three-ring segmented mirror. We first choose 36 random global piston positions that we draw from a uniform distribution such that the phase difference between any two adjacent segments can be any value that lies in the range $[-19\lambda_0, +19\lambda_0]$. At this point the wavefront can be seen as piece-wise constant with discontinuities at the segment edges.

The method requires the tip-tilt values of the segments to be detected and corrected previously. Another error source is then the residual tip-tilt that could remain after tip-tilt restoration. We add a small amount of those that we select randomly for any segment. This tip-tilt values change from segment to segment and from one simulation to the next. This helps the network to learn to detect piston values despite the unknown random small tip-tilt that could be present. The tip-tilt values for every segment are randomly selected from within the interval $\pm 0.0022''$. This means a difference of 10 nm between the vertex and the center of the segment. Tip-tilt restoration can be achieved with methods based on Curvature sensors [9] or through stacking. Higher precision can be obtain with more complex methods, e.g. active optics.

Table 1. Simulation parameters

Parameter	Value
Focal length of telescope	$f = 250$ m
Defocus distance	$l = 9$ m
Diameter of telescope	$D = 10.4$ m
Detector array size	1024×1024
Fried parameter	$r_0(@500nm) = 0.15$
Largest wavelength	$\lambda_0 = 700$ nm
Polishing error	$rms = 20$ nm
Tip-tilt error	$t_e = \pm 0.0022''$

We have considered as well the effect of the polishing errors in the surface of the mirrors. We created a phase screen using a Von Kármán spectrum with an outer scale of 0.2 m and $rms = 20$ nm. The screen so calculated is then added to the phase that we got in the previous step. This polishing error profile differs from one segment to the other but remains constant from one simulation to the next.

Once we have the wavefront, we proceed to compute the propagation a distance z by first applying Fresnel equation 3 followed by the square of the magnitude of the complex field. The propagation distance that we choose to meet the criteria 2 is $z = 6632.53$ m.

The size of the detector is an important issue too. We use the dimensions 1024×1024 which is a very standard size in astronomy. It allows the diffraction pattern created in the defocused plane to be well sampled by the detector.

In order to simulate the atmospheric conditions we filter the intensity image at the defocused plane with the long exposure transfer function of the atmosphere [10]. We randomly select a value for Fried parameter between 0.15 and 0.2 in every simulation.

To overcome the fundamental limit of 2π in the measurement range, we need to include simulations with the exact same piston and tip-tilt values for four different wavelengths [11]. That would represent four simultaneous acquisitions with different filters. We use $\lambda_0 = 700$ nm as the reference wavelength and three shorter ones to disambiguate $\lambda_1 = 0.930\lambda_0$, $\lambda_2 = 0.860\lambda_0$ and $\lambda_3 = 0.790\lambda_0$.

In every training step new simulated images like the one showed in figure 1 are created. We proceed then to crop every segment junctions. An example of this cutout is showed in dash line in the upper left side of the same figure. We flipped from left to right some junctions to get the same orientation in the Y-shape pattern in all of them. And finally stack all these data to make a five-dimensional array with the following shape that is going to be the input to the network:

$$batchSize \times seqLength \times cropHeight \times cropWidth \times wavelength, \quad (4)$$

where batchSize in the number of images like the one in figure 1 that are generated at every training step, seqLength is the index of a particular junction withing the simulated image, cropHeight and cropWidth are height and width of bounding box around every junction respectively, and wavelength is one of the four different wavelength images included in the simulations.

Every simulation has different atmospheric seeing and tip-tilt values from one another but the polish error profile is the same in all of them. This means that polish error profile has to be measure in the actual optical system first before training the network.

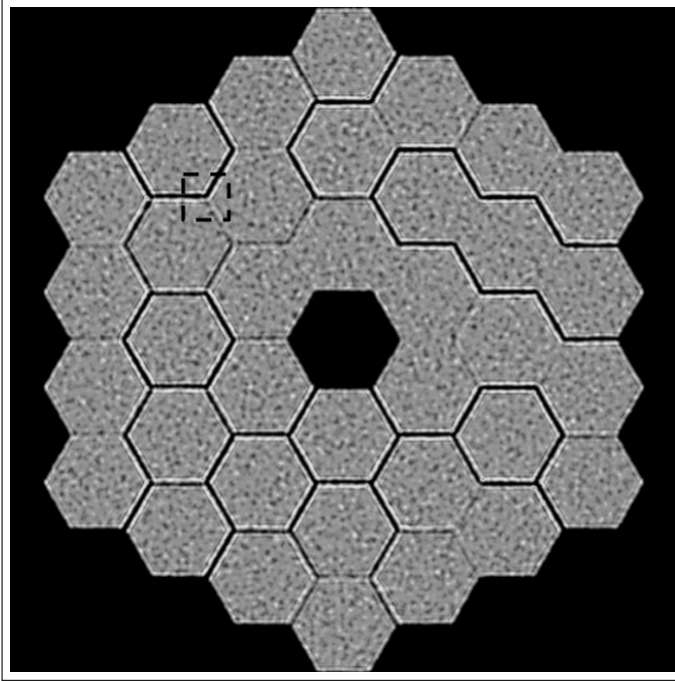


Fig. 1. Diffraction image from the simulations. Junction of three segments showed in dash line.

The network is trained in a fully supervised manner, that means that correct labels must be supplied together with the input data. The labels are not the global piston values themselves but the phase jumps between any two neighbouring segments.

The network architecture is roughly divided into two main branches. See diagram on figure 2 for clarity. One of the branches is trained to predict the ambiguity range the phase jump lies into. The other branch will be able to decide a floating value in the interval $[0, \pi]$ within that ambiguity range. So they deploy classification and regression tasks respectively. Both branches are based on a simple convolutional recurrent architecture with three convolutional layers [12] with ReLU activations followed by one bidirectional LSTM cell [13] and a fully connected layer to get the final scores.

The convolutional layers are able to extract the features from junction images that are useful to predict the piston values. These layers are specifically designed for dealing with data in a grid and take advantage of the spacial distribution. The recurrent layer takes the feature vectors produced by the convolutions and learns the relationship between junctions of different locations in the mirror. These layers are useful for handling sequences of data i.e. the sequence of junctions in the 36-segment mirror. These two paradigms combined give a robust and precise mechanism for predicting the targets. The prediction for a junction relies on the features contained in that particular junction image together with the features of all the other junctions of the sequence.

Diagram 2 shows an unwrapped version of the network, all blocks with same name means that they share weights between

them. It has two losses that are minimized simultaneously with mini-batch gradient descent and Adam update rule [14].

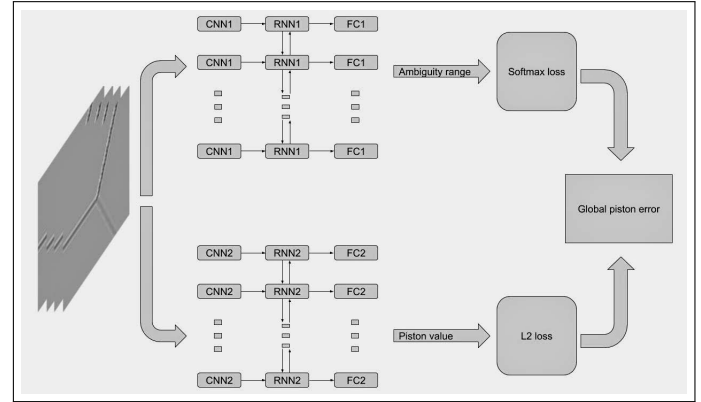


Fig. 2. Schematic representation of the network architecture.

The classification branch is trained by minimizing the softmax loss between predictions and ground truth labels. The span of each ambiguity range is π . Since the jumps between segments generated in the simulations allows them to be within $\pm 19\lambda_0$ means that every jump phase can belong to 76 different ambiguity ranges.

The regression branch is trained by minimizing the mean squared error between scores given by the network and actual phase jump values within one ambiguity range. It can be seen as the fine tuning of the prediction. In fact, this task can be achieved with the information contained in a single wavelength and shows better convergence properties than the classification branch. Same patterns should be assigned same label, it is taken into consideration the two periodicity properties that were mentioned previously in this paper.

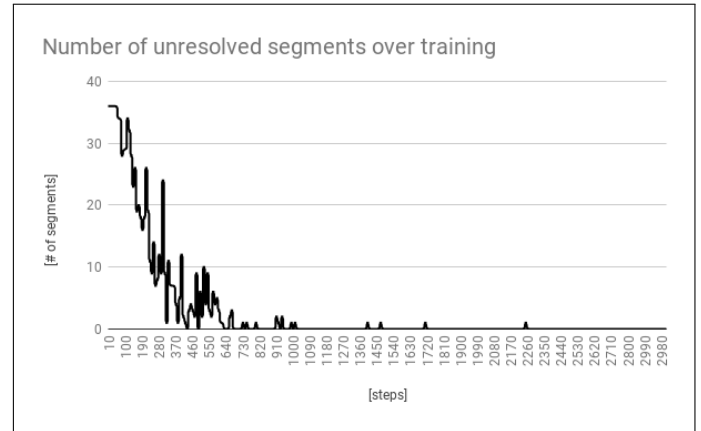


Fig. 3. Number of global piston values that cannot be resolved during training.

The network predicts three ambiguity ranges and three piston floating values for every junction image. We can combine these six predictions to get the three actual phase jumps among segments, i.e. to get phase jump floating values within the interval $\pm 19\lambda_0$. The set of all phase jump predictions for all adjacent segments form an overdetermined linear system of equations, $Ax = b$, where the unknowns are the global piston values measured with respect to one of the segments. We can find these

global piston values by solving the system through singular value decomposition. But before we should check the consistency of the predictions. One way of doing that is knowing that the three phase jumps of every junction must sum up to zero. If the summation of these three values are not close to zero or below some threshold, the predictions for these junction are not included in A . The rank of the matrix A will tell the number of segments that are not going to be able to be resolved with SVD.

In figure 3 it is plotted the number of global piston values that cannot be solved from the predictions. It displays the value every ten training steps. At every step the network analyses a whole sequence of junctions from a mirror instance like the one in figure 1. It only needs 1000 of such images to be able to solve global piston values for all segments at once. The error rate gets lower over time. Finally, it is found that only one segment was unresolved in the last 100 trials.

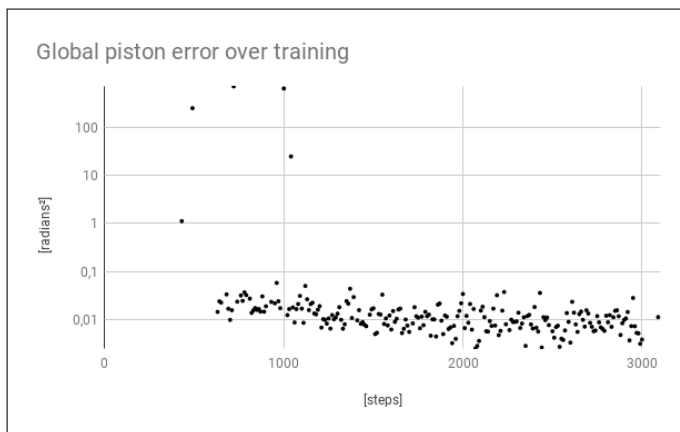


Fig. 4. Global piston error over training in logarithmic scale.

Only in the case of it being able to resolve all segments, it makes sense to compute the mean square error between the global piston values and ground truth values that were initially used in the simulations. Figure 4 shows these error values only when none of the segments was unresolved. This is the reason why the first part of the graph is empty. We can observe some outliers data points as well. These only happen at the beginning of the training because some errors bypass the consistency check due to the general instability of the predictions.

It has been shown in this paper a robust and reliable way of measuring global piston values in a segmented mirror. Several sources of errors were added to the simulations to test the robustness such as atmospheric turbulence, tip-tilt residuals and polishing errors. Only four visible wavelengths are needed for this method in order to operate, so no special hardware is needed.

It is really fast after the network is fully trained since it only takes one single forward pass of the network to predict the piston values. So it can be used at any time during the observation. The capture range achieved with this procedure is $13.3\ \mu\text{m}$ which might not be wide enough for phasing segments after replacements but for keeping track of the drift nightly and crosschecking measurements of other methods [15]. However capture range could be broadened by adding more wavelengths to the training.

The classification errors that we found were virtually zero after training for enough time. Moreover, this errors can be detected by the algorithm in advance to know which of the

segments are unresolved in any trial.

The accuracy of the global piston values measured with this method was around $\pm 11.14\ \text{nm}$. That result suffices for the adaptive optics system to work properly. All piston values referenced in this paper are measured at the wavefront.

ACKNOWLEDGEMENTS

This work was supported by the Spanish Ministry of Economy under the project DPI2015-66458-C2-2-R and by ERDF funds from the European Commission.

REFERENCES

1. G. Chanan, C. Ohara, and M. Troy, Appl. Opt. **39**, 4706 (2000).
2. G. Chanan, M. Troy, F. Dekens, S. Michaels, J. Nelson, T. Mast, and D. Kirkman, Appl. Opt. **37**, 140 (1998).
3. J. M. Rodríguez-Ramos and J. J. Fuensalida, "Piston detection of a segmented mirror telescope using a curvature sensor: preliminary results with numerical simulations," in *Optical Telescopes of Today and Tomorrow*, vol. 2871 (International Society for Optics and Photonics, 1997), pp. 613–617.
4. V. G. Orlov, S. Cuevas, F. Garfias, V. V. Voitsekhovich, and L. J. Sanchez, "Co-phasing of segmented mirror telescopes with curvature sensing," in *Telescope Structures, Enclosures, Controls, Assembly/Integration/Validation, and Commissioning*, vol. 4004 (International Society for Optics and Photonics, 2000), pp. 540–552.
5. P. C. McGuire, D. G. Sandler, M. Lloyd-Hart, and T. A. Rhoadarmer, "Adaptive optics: Neural network wavefront sensing, reconstruction, and prediction," in *Scientific Applications of Neural Nets*, (Springer, 1999), pp. 97–138.
6. D. Guerra-Ramos, L. Díaz-García, J. Trujillo-Sevilla, and J. M. Rodríguez-Ramos, Opt. letters **43**, 4264 (2018).
7. J. M. Rodríguez-Gonzalez and J. J. Fuensalida, "Diffractional treatment of curvature sensing in segmented-mirror telescopes," in *Large Ground-based Telescopes*, vol. 4837 (International Society for Optics and Photonics, 2003), pp. 726–737.
8. A. Schumacher and N. Devaney, Mon. Notices Royal Astron. Soc. **366**, 537 (2006).
9. J. J. Fernández-Valdivia, A. L. Sedano, S. Chueca, J. S. Gil, and J. M. Rodríguez-Ramos, Opt. Eng. **52**, 056601 (2013).
10. D. L. Fried, JOSA. **56**, 1372 (1966).
11. M. G. Lofdahl and H. Eriksson, Opt. Eng. **40**, 984 (2001).
12. A. Krizhevsky, I. Sutskever, and G. E. Hinton, "Imagenet classification with deep convolutional neural networks," in *Advances in neural information processing systems*, (2012), pp. 1097–1105.
13. S. Hochreiter and J. Schmidhuber, Neural computation **9**, 1735 (1997).
14. D. P. Kingma and J. Ba, arXiv preprint arXiv:1412.6980 (2014).
15. N. Yaitskova, F. Gonté, F. Derie, L. Noethe, I. Surdej, R. Karban, K. Dohlen, M. Langlois, S. Esposito, E. Pinna *et al.*, "The active phasing experiment: Part i. concept and objectives," in *Ground-based and Airborne Telescopes*, vol. 6267 (International Society for Optics and Photonics, 2006), p. 62672Z.

FULL REFERENCES

1. G. Chanan, C. Ohara, and M. Troy, "Phasing the mirror segments of the keck telescopes ii: the narrow-band phasing algorithm," *Appl. Opt.* **39**, 4706–4714 (2000).
2. G. Chanan, M. Troy, F. Dekens, S. Michaels, J. Nelson, T. Mast, and D. Kirkman, "Phasing the mirror segments of the keck telescopes: the broadband phasing algorithm," *Appl. Opt.* **37**, 140–155 (1998).
3. J. M. Rodríguez-Ramos and J. J. Fuensalida, "Piston detection of a segmented mirror telescope using a curvature sensor: preliminary results with numerical simulations," in *Optical Telescopes of Today and Tomorrow*, , vol. 2871 (International Society for Optics and Photonics, 1997), pp. 613–617.
4. V. G. Orlov, S. Cuevas, F. Garfías, V. V. Voitsekhovich, and L. J. Sanchez, "Co-phasing of segmented mirror telescopes with curvature sensing," in *Telescope Structures, Enclosures, Controls, Assembly/Integration/Validation, and Commissioning*, , vol. 4004 (International Society for Optics and Photonics, 2000), pp. 540–552.
5. P. C. McGuire, D. G. Sandler, M. Lloyd-Hart, and T. A. Rhoadarmer, "Adaptive optics: Neural network wavefront sensing, reconstruction, and prediction," in *Scientific Applications of Neural Nets*, (Springer, 1999), pp. 97–138.
6. D. Guerra-Ramos, L. Díaz-García, J. Trujillo-Sevilla, and J. M. Rodríguez-Ramos, "Piston alignment of segmented optical mirrors via convolutional neural networks," *Opt. letters* **43**, 4264–4267 (2018).
7. J. M. Rodríguez-Gonzalez and J. J. Fuensalida, "Diffractional treatment of curvature sensing in segmented-mirror telescopes," in *Large Ground-based Telescopes*, , vol. 4837 (International Society for Optics and Photonics, 2003), pp. 726–737.
8. A. Schumacher and N. Devaney, "Phasing segmented mirrors using defocused images at visible wavelengths," *Mon. Notices Royal Astron. Soc.* **366**, 537–546 (2006).
9. J. J. Fernández-Valdivia, A. L. Sedano, S. Chueca, J. S. Gil, and J. M. Rodríguez-Ramos, "Tip-tilt restoration of a segmented optical mirror using a geometric sensor," *Opt. Eng.* **52**, 056601 (2013).
10. D. L. Fried, "Optical resolution through a randomly inhomogeneous medium for very long and very short exposures," *JOSA.* **56**, 1372–1379 (1966).
11. M. G. Lofdahl and H. Eriksson, "Algorithm for resolving 2pi ambiguities in interferometric measurements by use of multiple wavelengths," *Opt. Eng.* **40**, 984–991 (2001).
12. A. Krizhevsky, I. Sutskever, and G. E. Hinton, "Imagenet classification with deep convolutional neural networks," in *Advances in neural information processing systems*, (2012), pp. 1097–1105.
13. S. Hochreiter and J. Schmidhuber, "Long short-term memory," *Neural computation* **9**, 1735–1780 (1997).
14. D. P. Kingma and J. Ba, "Adam: A method for stochastic optimization," *arXiv preprint arXiv:1412.6980* (2014).
15. N. Yaitskova, F. Gonte, F. Derie, L. Noethe, I. Surdej, R. Karban, K. Dohlen, M. Langlois, S. Esposito, E. Pinna *et al.*, "The active phasing experiment: Part i. concept and objectives," in *Ground-based and Airborne Telescopes*, , vol. 6267 (International Society for Optics and Photonics, 2006), p. 62672Z.